

# Extended Emission from the PSR B1259-63/SS 2883 Binary Detected with Chandra

George G. Pavlov<sup>1,2</sup>, Chulhoon Chang<sup>1</sup>, and Oleg Kargaltsev<sup>3</sup>

## ABSTRACT

PSR B1259–63 is a middle-aged radio pulsar ( $P = 48$  ms,  $\tau = 330$  kyr,  $\dot{E} = 8.3 \times 10^{35}$  erg s<sup>-1</sup>) in an eccentric binary ( $P_{\text{orb}} = 3.4$  yr,  $e = 0.87$ ) with a high-mass Be companion, SS 2883. We observed the binary near apastron with the *Chandra* ACIS detector on 2009 May 14 for 28 ks. In addition to the previously studied pointlike source at the pulsar’s position, we detected extended emission on the south-southwest side of this source. The pointlike source spectrum can be described by the absorbed power-law model with the hydrogen column density  $N_{\text{H}} = (2.5 \pm 0.6) \times 10^{21}$  cm<sup>-2</sup>, photon index  $\Gamma = 1.6 \pm 0.1$ , and luminosity  $L_{0.5-8\text{keV}} \approx 1.3 \times 10^{33} d_3^2$  ergs s<sup>-1</sup>, where  $d_3$  is the distance scaled to 3 kpc. This emission likely includes an unresolved part of the pulsar wind nebula (PWN) created by the colliding winds from the pulsar and the Be companion, and a contribution from the pulsar magnetosphere. The extended emission apparently consists of two components. The highly significant compact component looks like a southward extension of the pointlike source image, seen up to  $\sim 4''$  from the pulsar position. Its spectrum has about the same slope as the pointlike source spectrum, while its luminosity is a factor of 10 lower. We also detected an elongated feature extended  $\sim 15''$  southwest of the pulsar, but significance of this detection is marginal. We tentatively interpret the resolved compact PWN component as a shocked pulsar wind blown out of the binary by the wind of the Be component, while the elongated component could be a pulsar jet.

*Subject headings:* pulsars: individual (PSR B1259–63) – stars: neutron – X-rays: binaries

## 1. Introduction

The outstanding resolution of *Chandra* has made possible detailed investigations of pulsar wind nebulae (PWNe). PWNe are formed by the relativistic pulsar wind (PW), which shocks in the ambient medium and emits synchrotron radiation. The PWN morphology depends on the Mach number,  $\mathcal{M} = v/c_s$ , where  $v$  is the pulsar’s velocity relative to the ambient medium, and  $c_s$  is the speed of sound. PWNe created by subsonically moving pulsars, such as the famous Crab,

exhibit “torus-jet” morphology, where the torus represents a shocked equatorial wind beyond the ring-like termination shock (TS), while the jets along the pulsar’s spin axis are polar outflows. At  $\mathcal{M} \gg 1$ , when the ram pressure exceeds the ambient pressure,  $p_{\text{ram}} = \rho_{\text{amb}} v^2 \gg p_{\text{amb}}$ , the TS acquires a bullet-like shape (Gaensler et al. 2004; Bucciantini et al. 2005), and the PWN exhibits a cometary bow-shock morphology, with a long tail behind the moving pulsar. Spectacular examples of such PWNe are created by the pulsars J1747–2958 (Gaensler et al. 2004) and J1509–5850 (Kargaltsev et al. 2008). The tails may coexist with pulsar jets, often aligned with the proper motion direction (e.g., Pavlov et al. 2003).

An interesting modification of bow-shock PWNe is expected when the pulsar is in a high-mass binary system. In such a system, the pulsar moves

<sup>1</sup>Department of Astronomy & Astrophysics, Pennsylvania State University, PA 16802, USA; pavlov@astro.psu.edu, chchang@astro.psu.edu

<sup>2</sup>St.-Petersburg State Polytechnical University, Polytekhnicheskaya ul., 29, 195251, Russia

<sup>3</sup>Department of Astronomy, University of Florida, FL 32611, USA; kargaltsev@astro.ufl.edu

in the wind emanating from the high-mass companion, and the bow-shock PWN is produced by the collision of the relativistic PW with the dense nonrelativistic wind of the companion (instead of the interstellar medium (ISM) in the case of a solitary pulsar). The overall appearance, luminosity, and spectrum of such a PWN depend on the ratio of the momentum fluxes carried by the winds, the velocities  $\vec{v}_w$  and  $\vec{v}_p$  of the companion's wind and the pulsar's orbital motion, the temperature and density of the companion's wind, the anisotropy of the outflows, and the separation between the pulsar and the companion (Tavani & Arons 1997, hereafter TA97). As these parameters vary along the orbit, the PWN's luminosity, spectrum, shape, size, and orientation should also vary. If such a PWN can be resolved, observations of the variable PWN morphology would allow a more definitive study of the wind properties than observations of an unresolved PWN + binary system.

A promising target for such studies is the well-known binary system PSR B1259–63/SS2883. PSR B1259–63 (hereafter B1259) is a middle-aged radio pulsar, with the period  $P = 47.8$  ms, spin-down age  $\tau = P/2\dot{P} = 330$  kyr, spin-down power  $\dot{E} = 8.3 \times 10^{35}$  ergs s $^{-1}$ , and magnetic field  $B = 3.3 \times 10^{11}$  G (Wang et al. 2004). It is in an eccentric, wide binary ( $P_{\text{bin}} = 1237$  d  $\approx 3.4$  yr,  $e = 0.87$ ,  $a \sin i = 3.9 \times 10^{13}$  cm,  $i \approx 36^\circ$ ; Johnston et al. 1992, 1994) with a 10th-magnitude Be star SS2883 ( $M_* \approx 10M_\odot$ ,  $R_* \approx 6R_\odot$ ; Johnston et al. 1994). The distance estimates based on the dispersion measure (DM = 147 pc cm $^{-3}$ ) give  $d = 4.6$  kpc for the model of the Galactic electron density distribution by Taylor & Cordes (1993), and  $d = 2.75^{+0.61}_{-0.49}$  kpc for the NE2001 model by Cordes & Lazio (2002). However, Johnston et al. (1994) place the system at  $d \approx 1.5$  kpc, in the Sagittarius arm, based on the properties of the optical companion. As the distance remains somewhat uncertain, we will scale it to 3 kpc below,  $d = 3 d_3$  kpc.

Discovered with *ROSAT* (Cominsky et al. 1994), X-ray emission from B1259 has been studied with *ASCA* (Kaspi et al. 1995; Hirayama et al. 1999), *Beppo-SAX* (Nicastro et al. 1998), *INTEGRAL* (Shaw et al. 2004), *XMM-Newton* (Chernyakova et al. 2006, 2009), *Suzaku* (Uchiyama et al. 2009), and *Swift* and *Chandra* (Chernyakova et al. 2009). TeV emission from this system near perias-

tron was detected with the HESS observatory (Aharonian et al. 2005, 2009). The multi-year observations have shown that its X-ray flux and spectrum vary with orbital phase. For instance, the 1–10 keV energy flux is at minimum,  $1.0 \times 10^{-12}$  erg cm $^{-2}$  s $^{-1}$  (i.e.,  $L_X = 1.1 \times 10^{33} d_3^2$  ergs s $^{-1}$ ) at apastron, while it is a factor of 20 higher nine days before periastron. The slope of its power-law (PL) spectrum also varies, from  $\Gamma \approx 1.7$  (at apastron) to 1.2 (25 days before periastron) to 2.0 (at periastron). No pulsations with the radio pulsar period have been detected from the system outside the radio range. The orbital variations of the X-ray flux and spectrum have been explained by a model in which the X-ray emission is generated in a PWN formed by the colliding winds; the PWN becomes more compact and luminous when the pulsar crosses the equatorial disk outflow (angular half-width of about  $20^\circ$ ) of the Be companion, tilted with respect to the orbital plane by an angle  $\sim 25^\circ$  (TA97; Chernyakova et al. 2006). There is no general consensus on the X-ray emission mechanism (synchrotron emission or inverse Compton (IC) scattering of companion's optical/UV photons).

It would be interesting to study the unusual PWN of B1259 in X-rays, but, at realistic wind parameters, the characteristic size of the TS surface ( $\lesssim 0''.01$ ) in the B1259 PWN is too small to resolve it even with *Chandra*. On the other hand, we know from the models of bow-shock PWNe and observations of supersonic solitary pulsars that the flow speed in the collimated tail behind the moving pulsar can be so high that the length of the observable part of the tail can exceed the characteristic TS size by a very large factor (Kargaltsev et al. 2008), despite the fast synchrotron and IC cooling of the emitting relativistic particles. The tail in the immediate vicinity of the binary should be oriented along the vector  $\vec{v}_w - \vec{v}_p$ , i.e., almost along the line connecting the Be star and the pulsar (as  $v_w \gg v_p$ ). The tail should rotate with the binary period, so that its large-scale appearance would resemble an Archimedes spiral (Dubus 2006). Optimal binary phases to search for the outflow are near the apastron, when the pointlike source emission is the faintest, and the size of the bow-shock PWN is the largest. We should note that the four *Chandra* observations taken near the periastron of 2007 (Chernyakova et al. 2009) were not suitable

for detecting extended emission because they were short (3–7 ks) and used either Continuous Clocking mode (which produces only one-dimensional image) or High Energy Transmission Grating. In addition to the tail outflow, a high-resolution image may show pulsar jets, which can penetrate through the companion’s wind, and whose orientation would not show any orbital dependence.

To search for extended X-ray emission from the PWN tail and pulsar jets, and to better understand the nature of stellar and pulsar winds and their interaction, we observed B1259 with *Chandra* near apastron of 2009. We describe this observation and the data analysis in Section 2, and discuss our results in Section 3.

## 2. Observations and Data Analysis

We observed B1259 with the Advanced CCD Imaging Spectrometer (ACIS) on board *Chandra* on 2009 May 14 (ObsID 10089), 39 days after apastron (i.e., at the binary phase  $\phi = 0.532$ , counted from periastron, or the true anomaly  $\theta = 181.63^\circ$ ). The target was observed for 28.28 ks in timed exposure mode using “very faint” telemetry format. To minimize the pile-up effects, we used a custom 124 pixel subarray and turned off all the ACIS chips but I3. The frame time in this configuration is 0.44104 s (0.4 s exposure time and 0.04104 s the image transfer time). The Y-offset of  $-0'.2$  and Z-offset of  $-0'.25$  put the target  $29''$  off-axis, at a distance of  $> 20''$  from the nearest boundary of the  $\approx 8' \times 1'$  field of view (FOV), with allowance for the  $8''$  amplitude dither. There were no significant flares during the observation. The useful scientific exposure time (livetime) was 25.65 ks. The data were reduced and analyzed with the *Chandra* Interactive Analysis Observations (CIAO) package (ver. 4.2), using CALDB 4.2.0. We used *Chandra* Ray Tracer (ChaRT)<sup>1</sup> and MARX<sup>2</sup> software for image analysis, and XSPEC (ver. 12.5.1) for spectral analysis.

### 2.1. Image Analysis

To produce images of the pulsar and its vicinity at subpixel resolution, we removed the pipeline pixel randomization and applied the subpixel res-

<sup>1</sup>See <http://cxc.harvard.edu/chart/threads/index.html>.

<sup>2</sup>See <http://space.mit.edu/CXC/MARX/>.

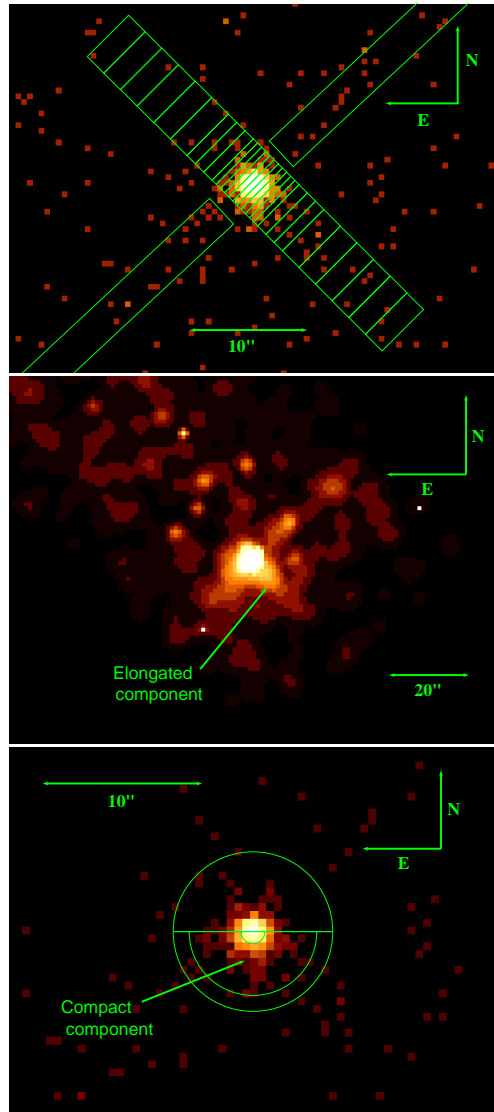


Fig. 1.— ACIS-I3 images of B1259. *Top*: Original (unbinned, unsmoothed) image in the 0.5–8 keV band. The  $3''$ -wide strips northwest and southeast of the pulsar are used for the analysis of the trailed image of the pointlike source. The  $36'' \times 5''$  rectangle northeast and southwest of the pulsar is used for the analysis of extended emission. *Middle*: The 0.5–8 keV image binned to a pixel size of  $0''.98$  and smoothed with *csmooth* to emphasize the extended emission. *Bottom*: Unbinned, unsmoothed image in the 1–7 keV band; the semicircles are used for the imaging and spectral analyses of extended emission (see text and Table 1).

olution tool to split-pixel events in the image (Mori et al. 2001; Tsunemi et al. 2001). Figure 1 shows images of the region around B1259 on the I3 chip in the 0.5–8 keV and 1–7 keV energy bands. The coordinates of the bright compact source at the image center (2050 counts in the  $1''.5$  radius aperture in the 0.5–8 keV band) are R.A.(J2000) =  $13^{\text{h}}02^{\text{m}}47^{\text{s}}.625$ , Decl.(J2000) =  $-63^{\circ}50'08''.38$ , as measured by the CIAO *wavdetect* tool. This position differs by  $0''.36$  from the radio pulsar position, R.A.(J2000) =  $13^{\text{h}}02^{\text{m}}47^{\text{s}}.65(1)$ , Decl.(J2000) =  $-63^{\circ}50'08''.7(1)$ , for the epoch MJD 50,357 (Wang et al. 2004); such a difference is within the uncertainty of the absolute *Chandra* astrometry (e.g.,  $0''.62$  at the 90% confidence level for sources within  $2'$  from the optical axis on the ACIS-I3 chip<sup>3</sup>).

In the image we see two extended structures apparently associated with the pulsar: a narrow linear structure seen on both sides of the pulsar along the northwest-southeast direction, and a one-sided south-southwest extension of point-like source image. As the linear structure is oriented along the CCD column direction, it could be naturally interpreted as the “trailed image” of the pointlike source, formed by the source photons arriving during the CCD charge transfer to the framestore region. To confirm this explanation and check that no additional extended emission is required to produce the observed structure, we measured the number of counts in a  $3''$ -wide strip, which goes parallel to the chip columns from one edge of the subarray to the other (excluding a  $7''$  gap with the pulsar in the middle; see the upper panel of Figure 1), and compared it with the number of counts expected in the trailed image. The background surface brightness,  $0.044$  counts arcsec<sup>-2</sup> in the 0.5–8 keV band, was estimated in a  $25''$  radius circle located about  $50''$  northeast from the pulsar. We found 44 counts in the strip, of which 9.2 counts belong to the background, i.e., there are  $34.8 \pm 6.7$  background-subtracted counts. The number of counts expected in the trailed image can be estimated as  $N_{\text{trail}} = C_{\text{src}} t_{\text{trail}} (n_{\text{strip}}/n_{\text{chip}}) = 22.5 \pm 0.6$ , where  $C_{\text{src}} = 79.9 \pm 1.8$  counts ks<sup>-1</sup> is the source count rate in the  $1''.5$  aperture,  $t_{\text{trail}} = 2.63$  ks is the

total image transfer time during the observation,  $n_{\text{strip}} = 110$  pixels is the strip length in chip coordinates, and  $n_{\text{chip}} = 1024$  pixels is the chip size. Although the number of counts detected in the strip exceeds  $N_{\text{trail}}$  by  $12.3 \pm 6.7$  counts, the statistical significance of the excess is low ( $1.8\sigma$ ), which means that the northwest-southeast linear structure is indeed the trailed image, without a significant contribution from an extended source.

To evaluate the statistical significance of the other extended feature (south-southwest of the pulsar, see Figure 1), we simulated an observation of a point source with the same properties as the observed ones using the ChaRT and MARX packages. To reduce the statistical errors of the simulation, we increased the exposure time to 200 ks when running ChaRT and then rescaled the image to compare with the data. We have also tried several values of the DitherBlur parameter of MARX to match the simulated point spread function (PSF) with the real data and found the best match at the value of  $0''.2$ .

The extended emission apparently consists of a compact part, which is seen up to about  $4''$  south of the pulsar, and a narrow elongated structure of about  $10''$ – $15''$  length southwest of the pulsar, which might bend northward at the apparent end. To estimate the significance of these structures, we investigated the count distributions in two semicircles of  $5''$  radius (north and south of the pulsar; see the bottom panel of Figure 1) and in the  $36'' \times 5''$  rectangular region (oriented in the northeast-southwest direction, i.e., along the elongated structure; see the top panel of Figure 1).

Figure 2 shows the observed and simulated radial distributions of counts in the northern and southern semicircles, in the 1–7 keV band. We see that in the northern semicircle the observed distribution is rather close to the simulated one, while in the southern semicircle there is a significant excess of the observed counts with respect to both the simulated distribution and the observed counts in the northern semicircle. For instance, for radii between  $0''.75$  and  $4''$ , the numbers of counts in the southern and northern semicircles are 276 and 160, respectively, i.e., the excess is  $116 \pm 21$  counts, significant at the  $5.6\sigma$  level.

Figure 3 shows the distribution of 0.5–8 keV counts along the length  $l$  of the  $36'' \times 5''$  rectangle ( $l = 0$  corresponds to the pulsar position;

<sup>3</sup>See Figure 5.4 in the *Chandra* Proposer’s Observatory Guide (POG), ver. 12 <http://cxc.harvard.edu/proposer/POG/>.

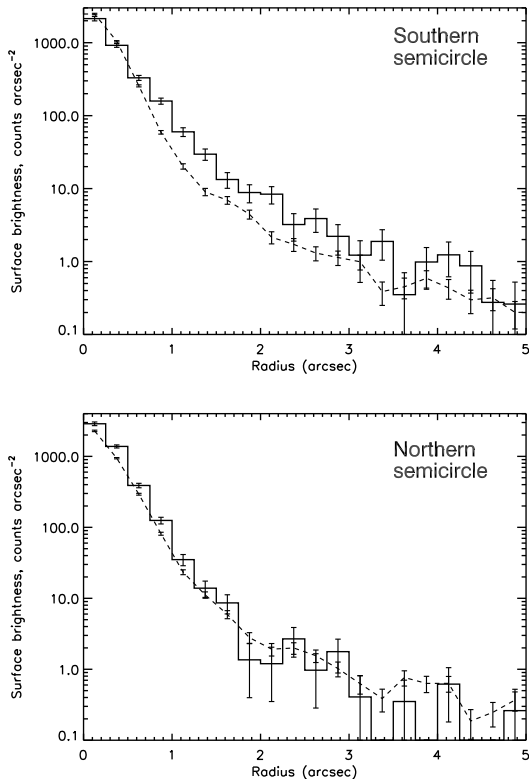


Fig. 2.— Observed radial count distributions (histograms) in the southern (top) and northern (bottom) semicircles (see the bottom panel in Figure 1), in the 1–7 keV band, are compared with the ChART + MARX simulation of a point source (dashed line).

$l > 0$  southwest of the pulsar). We see an excess of observed counts over the simulated profile in the southwest half of the rectangle. For instance, at  $1'' < l < 18''$  there are 158 counts; subtracting the contribution from the PSF tail and background (65.2 and 3.7 counts, respectively), we obtain the excess of  $89 \pm 13$  counts, significant at the  $6.9\sigma$  level (if only statistical uncertainties are taken into account). The difference between the numbers of observed counts in the rectangle segments symmetric with respect to the pulsar position confirms the excess. For instance, the difference of  $158 - 91 = 67 \pm 16$  counts between the  $1'' < l < 18''$  and  $-18'' < l < -1''$  is significant at the  $4\sigma$  level.

The count excess southwest of the pulsar is,

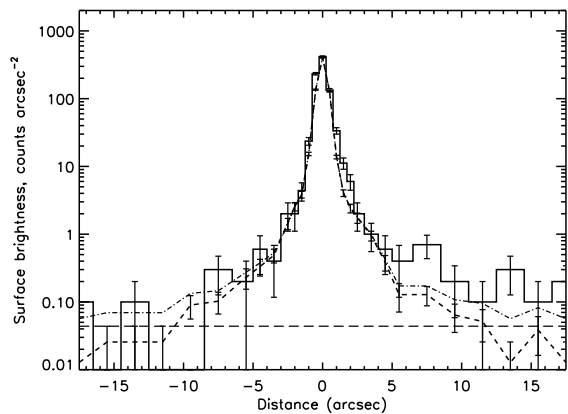


Fig. 3.— Observed count distribution (histogram) along the length of the  $36'' \times 5''$  rectangle shown in the top panel of Figure 1 (approximately in the northeast-southwest direction) is compared with the ChART+MARX simulation of a point source (dashed line). The positive and negative distances correspond to the southwest and northeast directions. The horizontal dashed line shows the background level ( $0.044 \text{ counts arcsec}^{-2}$ ), while the dash-dot line corresponds to the sum of the background and the simulation.

however, mostly due to the brightening in the immediate pulsar vicinity, at  $l \approx 1''\text{--}2''$ , while the statistical significance of the apparent excess at  $l > 5''$  (the alleged elongated component) is marginal. For instance, in the 1–7 keV band, we detected 15 and 3 counts in the  $5'' < l < 18''$  and  $-18'' < l < -5''$  segments, respectively, so that the difference,  $12.0 \pm 4.2$  counts, is significant at the  $2.9\sigma$  level, too low to firmly rule out a statistical fluctuation.

The presence of asymmetric extended emission at distances  $\gtrsim 1''$  from the pulsar is also supported by Figure 4, which shows the result of subtraction of the simulated point source image from the observed one. In addition to the asymmetric extended emission, the subtracted image shows some azimuthally asymmetric systematic residuals of both signs within  $\approx 1''$  from the point source position, resembling those reported recently by Juda & Karovska (2010) and Kashyap (2010)<sup>4</sup>. This means that the actual PSF core is

<sup>4</sup> We should note that the spatial structure of the residuals

different from the azimuthally symmetric model; this difference, however, makes no effect beyond  $1''$  from the point source position<sup>5</sup>.

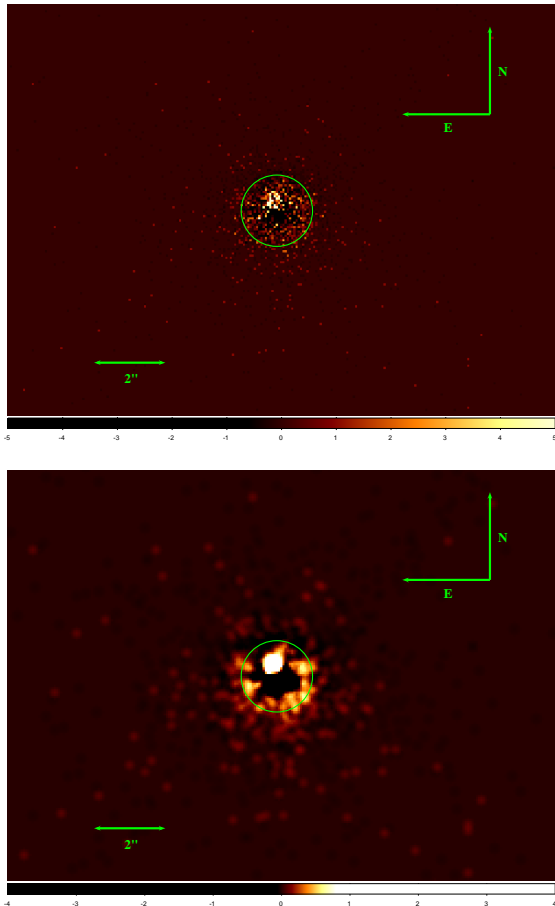


Fig. 4.— *Top*: ACIS-I3 image of B1259 with the simulated point source contribution subtracted. The ChART+MARX simulated image (with DitherBlur =  $0''.2$ ) was centered on the *wadetect* position (see Section 2.1). Both the observed and simulated images were rebinned to  $1/8$  of the original ACIS pixel size. The residual structure within the  $1''$  radius circle is caused by imperfections of the simulated PSF core (see Kashyap 2010). *Bottom*: The same image smoothed with the  $0''.19$  Gaussian kernel.

in Figure 4 differs significantly from that reported by these authors, but the structure strongly depends on the choice of the image center within the ACIS pixel.

<sup>5</sup>See [http://cxc.harvard.edu/ciao/caveats/psf\\_artifact.html#fig1](http://cxc.harvard.edu/ciao/caveats/psf_artifact.html#fig1).

In principle, an asymmetry of a point source image can be caused by the tilt of the innermost *Chandra* telescope mirrors (the mirror pair 6) with respect to the other mirrors (see Section 4.2.3 of POG, and Jerius et al. 2004). It has been observed in bright sources (e.g., the Vela pulsar; see Pavlov et al. 2001) as an image elongation between the  $-Z$  and  $+Y$  directions (in spacecraft coordinates). In our case, the extended emission is seen between the  $+Z$  and  $-Y$  directions. Moreover, the effect of the innermost mirror misalignment is significant for higher photon energies ( $E \gtrsim 5$  keV), while the asymmetry we observe in the B1259 image is about the same in the 0.5–1.75 and 1.75–8.0 keV images (which have approximately the same numbers of counts), and our spectrum has too few high-energy counts that could cause this asymmetry. Therefore, the observed one-sided extended emission is not an artefact caused by the mirror misalignment. We suggest that this emission can be interpreted as an extended PWN of B1259 and conclude that the compact component of this PWN, up to  $\sim 4''$  from the pulsar, is firmly detected, while a longer observation is needed to confirm the reality of the elongated component.

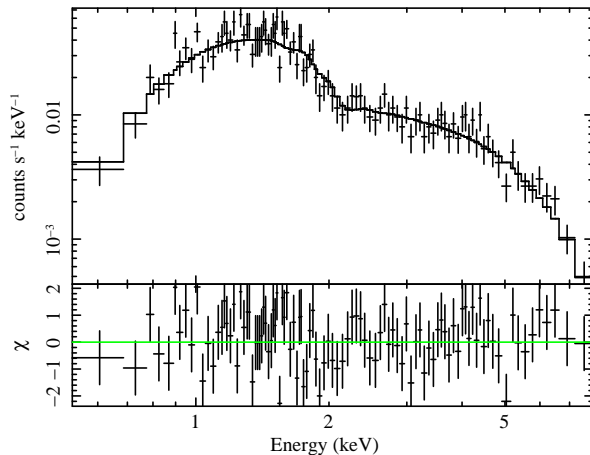


Fig. 5.— Spectrum of the pointlike source fitted with the absorbed PL model in the energy range of 0.5–8 keV.

## 2.2. Spectral Analysis

### 2.2.1. Pointlike source

For the spectral analysis of the pointlike source (which likely includes the unresolved part of the PWN, in addition to the pulsar), we extracted 1874 counts in the 0.5–8 keV band from a small circular aperture of 1'' radius. As the encircled count fraction is 88% for such an aperture and energy band (according to our ChaRT/MARX simulations), the aperture-corrected count rate is  $83.9 \pm 1.9$  counts  $\text{ks}^{-1}$ , or 0.034 counts per frame, which corresponds to a negligibly small pile-up fraction (about 1%, according to *Chandra* PIMMS<sup>6</sup>). The background contribution (0.14 counts) is negligible in such a small aperture. We binned the spectrum with minimum of 15 counts per bin and fit it with the absorbed PL model (see Figure 5). The fit is good ( $\chi^2_\nu = 0.99$  for 99 degrees of freedom); its results are reported in Table 1, while Figure 6 shows the confidence contours for the fitting parameters. The fit results are consistent with those obtained in an *XMM-Newton* observation near the 2002 apastron ( $N_{\text{H},21} = 2.9 \pm 0.2$ ,  $\Gamma = 1.69 \pm 0.04$ ,  $F = (1.04 \pm 0.49) \times 10^{-12}$  erg  $\text{cm}^{-2}$   $\text{s}^{-1}$  in the 1–10 keV band<sup>7</sup>; see Chernyakova et al. 2006) as well as with the *ROSAT* (Cominsky et al. 1994) and *ASCA* (Hirayama et al. 1999) near-apastron observations in 1992 and 1995, respectively.

### 2.2.2. Extended emission

It is difficult to measure the spectrum of the alleged PWN not only because of the small number of counts but also because the PWN emission region overlaps with the wings of the pulsar PSF. We, however, attempted to estimate the spectral slope and the flux of the PWN emission in the two regions shown in the bottom and top panels of Figure 1. First, using our ChaRT/MARX simulations, we extracted the PSF wing spectra in these regions and fit each of them with the absorbed PL model, freezing the hydrogen column density at the best-fit value obtained for the pointlike spectrum,  $N_{\text{H},21} = 2.5$  (see Table 1 for the fitting parameters). These spectra are slightly harder than

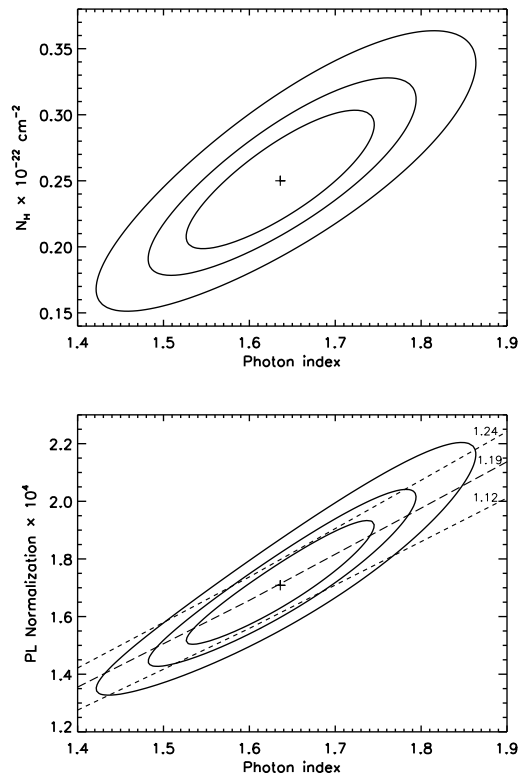


Fig. 6.— Confidence contours (68%, 90%, 99%) in the  $\Gamma$ - $N_{\text{H}}$  (*top*) and  $\Gamma$ - $\mathcal{N}$  (*bottom*) planes for the ACIS spectrum of the pointlike source, computed for the absorbed PL model. The PL normalization  $\mathcal{N}$  is in units of  $10^{-4}$  photons  $\text{cm}^{-2}$   $\text{s}^{-1}$  keV $^{-1}$  at 1 keV. The dashed lines are the lines of constant unabsorbed flux in the 0.5–8 keV band (the numbers near the lines are the flux values in units of  $10^{-12}$  erg  $\text{cm}^{-2}$   $\text{s}^{-1}$ ).

the PSF core spectrum because the PSF broadens with increasing energy. Extracting the background from the same regions that were used for the image analysis, we then fit the spectra in the two regions by the sums of two absorbed PL models (PSF wings + PWN), with  $N_{\text{H},21} = 2.5$  and the PSF wings model parameters frozen at the previously obtained best-fit values. We see from Table 1 that the spectra of the two regions have about the same slopes,  $\Gamma_{\text{pwn}} \approx 1.6$ , statistically indistinguishable from the slope of the pointlike source, while the PWN flux in the southern semi-annulus (S) is a factor of 3 higher than that in

<sup>6</sup>See <http://cxc.harvard.edu/toolkit/pimms.jsp>.

<sup>7</sup>Because of the relatively low angular resolution of *XMM-Newton*, those data include both the pointlike source and the extended emission.

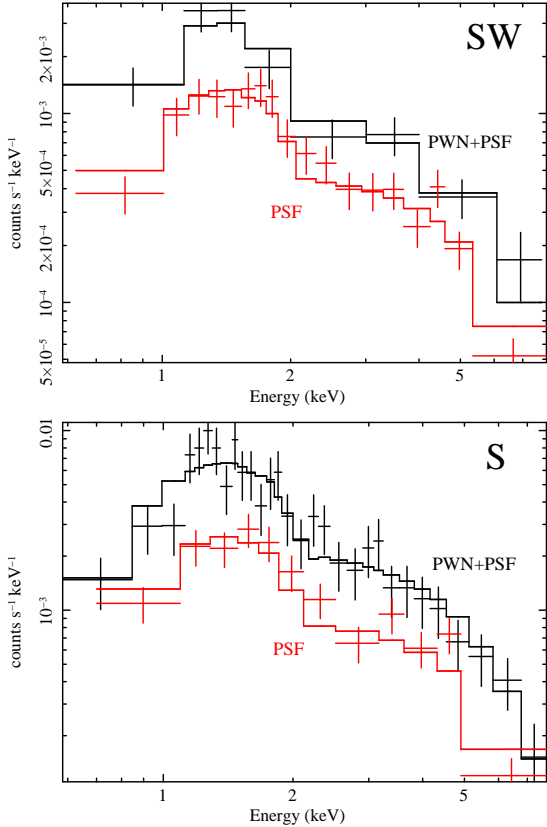


Fig. 7.— Spectra of the background-subtracted emission in the SW (*top*) and S (*bottom*) regions (see Table 1 and Figure 1). The red histograms show fits with the absorbed PL models of the corresponding PSF wing spectra obtained in the ChaRT+MARX simulations. The black histograms show fits of the observed (PSF+PWN) spectra with the sum of two absorbed PL models, one of which (with fixed parameters) describes the contribution of the PSF wings.

the southwest rectangle (SW). The total flux and the luminosity of the alleged PWN are a factor of  $\sim 10$  lower than those of the pointlike source.

### 3. Discussion

#### 3.1. Pointlike source

The pointlike source emission can include contributions from the pulsar, the Be companion, and the unresolved part of the PWN created by the colliding winds from the pulsar and the Be companion, including the ultracompact intrabinary PWN,

with a size smaller than the separation between the binary components,  $\lesssim 3d_3^{-1}$  milliarcseconds at apastron. Coronal emission from the Be companion, with an optically thin, thermal plasma spectrum corresponding to a temperature of a few million kelvins, might give some contribution in low-energy channels, but, given the goodness of the single-component PL fit, the contribution of the coronal emission can be neglected. The pulsar emission could include a thermal component, emitted from the neutron star surface, and a nonthermal component emitted from the pulsar’s magnetosphere. Since the observed spectrum excellently fits the single PL model, we conclude that the pulsar’s thermal emission is too soft and faint to be seen at the relatively large  $N_{\text{H}} \approx 2.5 \times 10^{21} \text{ cm}^{-2}$ . For instance, the thermal emission from the Geminga pulsar, whose spin-down age is similar to that of B1259 and whose bulk surface temperature is  $\lesssim 5 \times 10^5 \text{ K}$  (see, e.g., Kargaltsev et al. 2005), would be virtually undetectable at energies above 0.5 keV if Geminga were at the distance of B1259.

For a typical X-ray efficiency of the magnetospheric emission,  $\eta_{X,\text{psr}} \equiv L_{X,\text{psr}}/\dot{E} \sim 10^{-4}$  (see, e.g., Kargaltsev & Pavlov 2008), one would expect  $L_{X,\text{psr}} \sim 10^{32} \text{ erg s}^{-1}$ , which is an order of magnitude lower than the detected  $L_{0.5-8 \text{ keV}} = 1.3 \times 10^{33} d_3^2 \text{ erg s}^{-1}$ . However, as  $\eta_{X,\text{psr}}$  shows a large scatter (from  $< 10^{-5}$  to  $\sim 10^{-2}$  for pulsars with similar values of  $\dot{E}$  and  $\tau$  — see Kargaltsev & Pavlov 2009), the relatively high X-ray luminosity of B1259 does not rule out a substantial contribution from the pulsar, especially taking into account that the distance may be smaller than the assumed 3 kpc. As the magnetospheric emission is expected to be strongly pulsed, its contribution could be estimated by measuring X-ray pulsations near apastron. Such an attempt was made by Hirayama et al. (1999) in observations with the ASCA GIS detector, but the upper limit on the pulsed fraction,  $p_f \lesssim 40\%$ , was not constraining. To conclude, the pointlike emission likely includes contributions from the unresolved part of the PWN and the pulsar’s magnetosphere, with the total X-ray efficiency  $\eta_{0.5-8 \text{ keV}} = 1.6 \times 10^{-3} d_3^2$ . Timing observation with *XMM-Newton* or *Chandra* could help separate their contributions.



### 3.2. Extended emission

Thanks to the unprecedented angular resolution of *Chandra*, our observation of B1259 has revealed, for the first time, extended X-ray emission associated with this remarkable binary. As the X-ray emission with a PL spectrum is usually generated by relativistic particles, and the pulsar is the only natural source of such particles in B1259, we interpret the extended emission as a PWN.

The detected extended PWN emission appears to consist of two components. Firmly detected is only the relatively compact component south of the pulsar, with a characteristic size of  $\sim 4''$  and luminosity of  $\sim 10^{32} d_3^2 \text{ erg s}^{-1}$ . The detection of the less luminous elongated component, of  $\sim 15''$  length, is less certain.

The elongated component could be interpreted as a pulsar jet. Its  $\sim 15''$  angular length corresponds to  $\sim 7 \times 10^{17} \text{ cm}$  at  $d = 3 \text{ kpc}$ , which is comparable with the  $\sim 5 \times 10^{17} \text{ cm}$  and  $\sim 2 \times 10^{17} \text{ cm}$  projected lengths of the X-ray jets of the Vela and Geminga pulsars, respectively (Pavlov et al. 2003, 2010). Its luminosity,  $\sim 10^{31} \text{ erg s}^{-1}$ , is about  $10^{-5}$  of the pulsar’s spin-down power, versus  $\sim 10^{-6}$  for the Geminga and Vela pulsars. To check this interpretation, longer *Chandra* observations of B1259 are needed, at different binary phases. If the detected elongated feature is indeed the pulsar jet, we do not expect substantial variations in its luminosity and length, except may be for a short interval ( $\sim 40 \text{ d}$ ) around periastron, when accretion of the Be companion wind might quench the pulsar activity (Wang et al. 2004).

The compact PWN component could be associated with the shocked PW blown out of the binary by the wind of the Be companion. Similar to the case of a single pulsar moving in the ISM with a supersonic velocity, the collision of the two winds should create a bow shock within the binary (TA97) and a tail directed out of the binary approximately along the line connecting the Be companion with the pulsar<sup>8</sup>. As the pulsar moves along the binary orbit, the tail is expected to be bent in the direction opposite to the pulsar motion, resembling an Archimedes spiral (Dubus

2006). The tail’s shape can be described by the equation

$$R - R_p(\theta) = \frac{P_{\text{bin}}(1 - e^2)^{3/2}}{2\pi} \int_{\theta}^{\theta_p} \frac{V_{\text{flow}}(\theta')}{(1 + e \cos \theta')^2} d\theta', \quad (1)$$

where  $R$  and  $\theta$  are the radius and the azimuthal angle of a point on the tail’s central line in the reference frame centered at the Be companion,  $R_p$  and  $\theta_p$  are the radial coordinate and the true anomaly of the pulsar, and  $V_{\text{flow}}(\theta')$  is the flow speed that may vary along the tail. The shape of the tail near apastron, when  $|1 + \cos \theta| \ll 1$  and  $|1 + \cos \theta_p| \ll 1$ , is given by the following equation

$$\begin{aligned} R - R_p(\theta) &\approx \frac{P_{\text{bin}} \bar{V}_{\text{flow}} (1 + e)^{3/2}}{2\pi (1 - e)^{1/2}} (\theta_p - \theta) \\ &= 2.3 \times 10^{19} \frac{\bar{V}_{\text{flow}}}{c} \frac{\theta_p - \theta}{2\pi} \text{ cm}, \quad (2) \end{aligned}$$

where  $\bar{V}_{\text{flow}}$  is the average flow speed, and the numerical estimate is given for the B1259 case ( $\theta_p = 1.0090\pi$  for our observation). The compact PWN in the ACIS image looks like a one-sided bulge on (or a “blob” attached to) the pointlike source rather than a narrow tail. This is expected if the angular size of the visible tail only slightly exceeds the size of the PSF. In addition, the tail may significantly broaden by interactions with the ambient medium.

The luminosity of the compact component of the resolved PWN,  $L_{0.5-8 \text{ keV}} \sim 1.2 \times 10^{32} d_3^2 \text{ erg s}^{-1}$ , is a factor of  $\sim 10$  lower than the luminosity of the pointlike source, which includes the PWN and pulsar contributions in an unknown proportion. The corresponding X-ray efficiency,  $\eta_{0.5-8 \text{ keV}} = L_{0.5-8 \text{ keV}} / \dot{E} = 1.4 \times 10^{-4} d_3^2$ , is at the lower end of those observed in the tails of supersonically moving solitary pulsars (see Table 5 in Kargaltsev et al. 2008), but one should take into account that a substantial part of the alleged tail of B1259 cannot be resolved even with *Chandra*, so the true tail luminosity and the X-ray efficiency may be considerably larger than these estimates.

The observed angular size of the compact PWN,  $\sim 4''$ , which corresponds to the projected length of  $\sim 2 \times 10^{17} d_3 \text{ cm}$ , and the fact that the PWN is seen only on one side of the pulsar, put a constraint on the average flow speed:  $\bar{V}_{\text{flow}} \gtrsim 0.1c$ . Such high flow speeds have been obtained in numerical models for tails of bow-shock PWNs of

<sup>8</sup>We assume here that the pulsar’s velocity (which varies from  $12 \text{ km s}^{-1}$  at apastron to  $176 \text{ km s}^{-1}$  at periastron) is much smaller than the velocity of the Be companion’s wind near the pulsar (see TA97).

solitary pulsars (e.g.,  $V_{\text{flow}} \sim 0.1c\text{--}0.3c$  in the narrow central channel of the tail, and  $\sim 0.8c\text{--}0.9c$  in the tail’s “sheath”, in the models by Bucciantini et al. 2005), but these speeds may become lower at large distances from the pulsar because of the interaction with the ambient medium (this effect was not included in the numerical models). Observations of tails behind supersonically moving solitary pulsars also show rather high flow speeds — for instance,  $\bar{V}_{\text{flow}} \gtrsim 0.02c$  for the 6 pc tail behind PSR J1509–5850 (Kargaltsev et al. 2008).

Even higher flow speeds, corresponding to bulk motion Lorentz factors  $\gamma_{\text{bulk}}$  up to  $\sim 100$ , were obtained by Bogovalov et al. (2008) in hydrodynamical simulations of flows produced by the collision of the relativistic (pulsar) and nonrelativistic (Be star) winds in a binary system. The ultrarelativistic flows are formed when the ratio  $\eta$  of the momentum flux from the pulsar to that from the Be star exceeds  $1.25 \times 10^{-2}$ , in which case the TS surface becomes “unclosed” (i.e., the back surface of the TS bullet disappears). In the case of B1259,  $\eta$  may vary between  $\sim 10^{-2}$  and  $\sim 1$  along the binary orbit, being as large as 0.1–1 around apastron (when the PW interacts with the so-called polar component of the Be star outflow). If the confined flow indeed reaches such high speeds, it can penetrate farther into the ambient medium, which makes the suggested interpretation of the observed asymmetric emission even more plausible. Dubus et al. (2010) note that the properties of the observed X-ray and VHE emission from B1259 are not compatible with the strong Doppler boosting corresponding to such large  $\gamma_{\text{bulk}}$ . However, it is possible that, while the bulk of the observed high-energy emission is generated within (or very close to) the binary, where the flow is only mildly relativistic, the extended emission is generated by electrons supplied by the accelerated flow that slows down at large distances from the binary.

The interpretation of the compact PWN as a shocked PW outside the binary can constrain the wind parameters in various models of B1259. The X-ray PWN emission could be due to synchrotron radiation of ultrarelativistic electrons, accelerated at the inner shock front within the binary (TA97). To generate X-ray photons,  $E \gtrsim 0.5$  keV, the electron energy  $\gamma mc^2$  and the magnetic field  $B$  should be high enough:  $B\gamma^2 \gtrsim 10^{11}$  (where

$B$  is in units of gauss). On the other hand, the cooling time,  $t_{\text{cool}}$ , for the relativistic electrons in the flow should be longer than the flow time,  $t_{\text{flow}} \sim R/\bar{V}_{\text{flow}} \sim 3 \times 10^7 R_{17} V_{9.5}^{-1}$  s, where  $R_{17} = R/(10^{17} \text{ cm})$ ,  $V_{9.5} = \bar{V}_{\text{flow}}/(10^{9.5} \text{ cm s}^{-1})$ . Generally, both the synchrotron cooling in the magnetic field and IC cooling in the radiation field of the Be companion can be important. At the very high energies of electrons emitting synchrotron X-rays,  $\gamma \gg mc^2/\epsilon \sim 10^5$  (where  $\epsilon \sim 3kT_{\text{eff}} \sim 5$  eV is the mean photon energy), the IC cooling occurs in the Klein-Nishina regime. The IC cooling rate in this regime is much lower than in the Thomson regime:  $\dot{\gamma}_{\text{IC,KN}}/\dot{\gamma}_{\text{IC,T}} \sim (mc^2/\gamma\epsilon)^2 \ln(\gamma\epsilon/mc^2) \sim 10^{-4} \gamma_7^{-2} (\ln \gamma_7 + 5)$ , and it is much lower than the synchrotron cooling rate beyond the binary orbit. Therefore, the cooling time is determined by synchrotron radiation,  $t_{\text{cool}} \sim t_{\text{syn}} \sim 5 \times 10^8 \gamma^{-1} B^{-2}$  s, and it exceeds the flow time at  $\gamma B^2 < 16 V_{9.5} R_{17}^{-1}$ . Taking into account the condition  $B\gamma^2 \gtrsim 10^{11}$  derived above, we obtain

$$\begin{aligned} B &< 1.4 \times 10^{-3} V_{9.5}^{2/3} R_{17}^{-2/3} \text{ G}, \\ \gamma &> 0.9 \times 10^7 V_{9.5}^{-1/3} R_{17}^{1/3}, \end{aligned} \quad (3)$$

for the typical magnetic field and Lorentz factor. The upper limit on magnetic field is much lower than the magnetic field in the ultracompact intrabinary PWN (e.g.,  $B \sim 1$  G in the TA97 model), while the lower limit on Lorentz factor is close to  $\gamma_{\text{max}}$  of the electron energy spectrum in the shocked (uncooled) PW within the binary (TA97). To reconcile such high energies and low magnetic fields with the intrabinary PWN models, one has to assume that the radiating electrons are additionally accelerated in the tail, in some internal shocks or via magnetic field reconnection that transforms the magnetic field energy into the kinetic energy of particles.

As noted by Chernyakova et al. (2006, 2009), the TA97 model cannot explain some of the observed properties of the B1259’s radiation (such as the hardening of the X-ray spectrum near periastron). These authors (see also Neronov & Chernyakova 2007) discuss another model (first considered by Chernyakova & Illarionov 1999), in which the X-ray emission is generated by the IC scattering of stellar photons off moderately relativistic electrons with Lorentz factors  $\gamma \sim 10\text{--}100$  (much lower than in the TA97 model). As such scattering occurs in the Thomson regime, the cool-

ing rate is  $\dot{\gamma}_{\text{IC}} = -(4/3)(\sigma_{\text{T}}c/mc^2)\gamma^2 U_{\text{ph}}$ , where  $U_{\text{ph}} = L_*/(4\pi cR^2) = 1.7 \times 10^4 L_{*,38} R_{17}^{-2}$  eV cm<sup>-3</sup> is the photon energy density at the distance  $R = 10^{17} R_{17}$  cm from the Be companion (approximately equal to the distance from the binary at  $R \gg a$ ), and  $L_* = 10^{38} L_{*,38}$  erg s<sup>-1</sup> is the luminosity of the stellar companion. At realistic values of the magnetic field,  $B \lesssim 800 L_{*,38} R_{17}^{-1}$   $\mu\text{G}$ , the photon energy density exceeds the magnetic energy density, so the IC cooling is more efficient. Taking into account that  $\dot{\gamma}_{\text{IC}} \propto R^{-2}$ , the electron's energy at distance  $R$  is given by the equation

$$\gamma(R) = \gamma_0 \left[ 1 + \frac{\gamma_0}{\gamma_c} \left( 1 - \frac{R_0}{R} \right) \right]^{-1}, \quad (4)$$

where  $\gamma_0 = \gamma(R_0)$ ,  $\gamma_c = 3\pi mc^2 R_0 V_{\text{flow}} / (\sigma_{\text{T}} L_*) \approx 3.7 \times 10^4 R_{0,14} V_{9.5} L_{*,38}^{-1}$ . If we assume  $\gamma_0 \sim 10$ – $100$  close to the binary orbit at apastron ( $R_0 \sim 10^{14}$  cm), then  $\gamma_0/\gamma_c \sim (3$ – $30) \times 10^{-4} V_{9.5}^{-1}$ , which means that the total relative energy loss by an electron,  $(\gamma_0 - \gamma_\infty)/\gamma_0 = (\gamma_0/\gamma_c)[1 + (\gamma_0/\gamma_c)]^{-1} \approx \gamma_0/\gamma_c$ , is very small at realistic  $V_{\text{flow}} \gg 10$ – $100$  km s<sup>-1</sup>. Moreover, the upper limit on the X-ray efficiency of the resolved PWN between distances  $R_1$  and  $R_2$  from the binary,  $[\gamma(R_1) - \gamma(R_2)]/\gamma_0 \sim (\gamma_0/\gamma_c) R_0 (R_1^{-1} - R_2^{-1}) \sim 10^{-6} (\gamma_0/30) V_{9.5}^{-1} (R_{1,17}^{-1} - R_{2,17}^{-1})$ , is much smaller than the observed value,  $\sim 10^{-4}$ . This means that the observed extended X-ray emission cannot be explained by the IC scattering, and the synchrotron emission of electrons with TeV energies is a more plausible interpretation.

The suggested interpretation of the compact PWN as a bent tail of the shocked PW blown out of the binary by the wind of the Be companion implies that the compact PWN rotates around the pointlike source with the binary period, and its size and luminosity should depend on binary phase. This can be verified by observing this system with *Chandra* at different binary phases.

If these observations show the compact PWN at the same position with respect to the pulsar, another interpretation would be required to explain the extended emission. In principle, it might be a tail or trail of shocked PW behind the moving binary blown out by the head-on wind of the ambient ISM matter. The proper motion of B1259 has not been measured yet, but the speed of the high-mass binary should be much lower than that

of a solitary pulsar, so that it would be hard to explain even so short tail/trail as caused by the motion of B1259 in the ISM.

Finally, we note that strong evidence of extended emission around another  $\gamma$ -ray binary, the microquasar LS 5039, has been recently found in a *Chandra* ACIS observation (Durant et al. 2011). It shows that the compact object in LS 5039 is likely a rotation-powered pulsar rather than an accreting neutron star or a black hole. It also means that B1259 is not the only high-mass X-ray binary surrounded by an extended PWN.

We thank Nicholas Lee and the CXC Calibration team for the discussion of the mirror misalignment effect on ACIS images, and Maria Chernyakova for the discussion of the *XMM-Newton* spectrum of B1259 near apastron. We also thank the anonymous referee, whose remarks has allowed us to improve the presentation. Support for this work was provided by the National Aeronautics and Space Administration through *Chandra* Award Number GO9-0070X issued by the *Chandra* X-ray Observatory Center, which is operated by the Smithsonian Astrophysical Observatory for and on behalf of the National Aeronautics Space Administration under contract NAS8-03060. The work was also partially supported by NASA grants NNX09AC84G and NNX09AC81G, and NSF grants No. 0908733 and 0908611. The work by GGP was partly supported by the Ministry of Education and Science of the Russian Federation (Contract No. 11.G34.31.0001).

## REFERENCES

- Aharonian, F., et al. 2005, *A&A*, 442, 1
- Aharonian, F., et al. 2009, *A&A*, 507, 389
- Bogovalov, S. V., Khangulyan, D. V., Koldoba, A. V. Ustyugova, G. V., & Aharonian, F. A. 2008, *MNRAS*, 387, 63
- Bucciantini, N., Amato, E., & Del Zanna, L. 2005, *A&A*, 434, 189
- Chernyakova, M. A., & Illarionov, A. F. 1999, *MNRAS*, 304, 359
- Chernyakova, M., Neronov, A., Lutovinov, A., Rodriguez, J., & Johnston, S. 2006, *MNRAS*, 367, 1201

- Chernyakova, M., Neronov, A., Aharonian, F., Uchiyama, Y., & Takahashi, T. 2009, MNRAS, 397, 2126
- Cominsky, L., Roberts, M., & Johnston, S. 1994, ApJ, 427, 978
- Cordes, J. M., & Lazio, T. J. W. 2002, arXiv:astro-ph/0207156
- Dubus, G. 2006, A&A, 456, 801
- Dubus, G., Cerutti, B., & Henri, G. 2010, A&A, 516, A18
- Durant, M., Kargaltsev, O., Pavlov, G. G., & Garmire, G. P. 2011, ApJ, submitted
- Gaensler, B. M., van der Swaluw, E., Camilo, F., Kaspi, V. M., Baganoff, F. K., Yusef-Zadeh, F., & Manchester, R. N. 2004, ApJ, 616, 383
- Hirayama, M., Cominsky, L. R., Kaspi, V. M., Nagase, F., Tavani, M., Kawai, N., & Grove, J. E. 1999, ApJ, 521, 718
- Jerius, D. H., Gaetz, T. J., & Karovska, M. 2004, Proc. SPIE, 5165, 433
- Johnston, S., Manchester, R. N., Lyne, A. G., Bailes, M., Kaspi, V. M., Guojun, Q., & D'Amico, N. 1992, ApJ, 387, L41
- Johnston, S., Manchester, R. N., Lyne, A. G., Nicastro, L., & Spyromilio, J. 1994, MNRAS, 268, 430
- Juda, M., & Karovska, M. 2010, BAAS, 41, 722; <http://hea-www.harvard.edu/~juda/memos/HEAD2010/HEAD2010-poster.html>
- Kargaltsev, O. Y., & Pavlov, G. G. 2008, in AIP Conf. Proc. 983, 40 Years of Pulsars: Millisecond Pulsars, Magnetars, and More, ed. C. G. Bassa et al. (Melville, NY: AIP), 171
- Kargaltsev, O., & Pavlov, G. G. 2009, ApJ, 702, 433
- Kargaltsev, O., Pavlov, G. G., & Garmire, G. P. 2007, ApJ, 660, 1413
- Kargaltsev, O. Y., Pavlov, G. G., Zavlin, V. E., & Romani, R. W. 2005, ApJ, 625, 307
- Kargaltsev, O., Misanovic, Z., Pavlov, G. G., Wong, J. A., & Garmire, G. P. 2008, ApJ, 684, 542
- Kashyap, V. 2010, [http://cxc.harvard.edu/cal/Hrc/PSF/acis\\_psf\\_2010oct.html](http://cxc.harvard.edu/cal/Hrc/PSF/acis_psf_2010oct.html)
- Kaspi, V. M., Tavani, M., Nagase, F., Hirayama, M., Hoshino, M., Aoki, T., Kawai, N., & Arons, J. 1995, ApJ, 453, 424
- Mori, K., Tsunemi, H., Miyata, E., Baluta, C. J., Burrows, D. N., Garmire, G. P., & Chartas, G. 2001, in ASP Conf. Ser. 251, New Century of X-Ray Astronomy, ed. H. Inoue & H. Kunieda (San Francisco:ASP), 576
- Neronov, A., & Chernyakova, M. 2007, Astrophys. Space Sci., 309, 253
- Nicastro, L., dal Fiume, D., Orlandini, M., Cusumano, G., Sacco, B., Campana, S., Tavani, M., & Becker, W. 1998, in Neutron Stars and Pulsars: Thirty Years after the Discovery, eds. N. Shibasaki et al. (Tokyo: Univ. Acad. Press), 525
- Pavlov, G. G., Bhattacharyya, S., & Zavlin, V. E. 2010, ApJ, 715, 66
- Pavlov, G. G., Kargaltsev, O., Sanwal, D., & Garmire, G. P. 2001, ApJ, 554, L189
- Pavlov, G. G., Teter, M. A., Kargaltsev, O., & Sanwal, D. 2003, ApJ, 591, 1157
- Shaw, S. E., Chernyakova, M., Rodriguez, J., Walter, R., Kretschmar, P., & Mereghetti, S. 2004, A&A, 426, L33
- Tavani, M., & Arons, J. 1997, ApJ, 477, 439
- Taylor, J. H., & Cordes, J. M. 1993, ApJ, 411, 674
- Tsunemi, H., Mori, K., Miyata, E., Baluta, C. J., Burrows, D. N., Garmire, G. P., & Chartas, G. 2001, ApJ, 554, 496
- Uchiyama, Y., Tanaka, T., Takahashi, T., Mori, K., & Nakazawa, K. 2009, ApJ, 698, 911
- Wang, N., Johnston, S., & Manchester, R. N. 2004, MNRAS, 351, 599

Table 1: Properties of X-ray Emission from B1259

Region <sup>a</sup>	$N_{\text{H},21}$	$\Gamma$	$\mathcal{N}_{-6}^{\text{b}}$	$F_{-14}^{\text{c}}$	$F_{-14}^{\text{unabsd}}$	$L_{32}^{\text{e}}$
Pointlike	$2.50^{+0.60}_{-0.54}$	$1.64^{+0.12}_{-0.11}$	$171^{+26}_{-22}$	$83.0 \pm 4.5$	$119^{+6}_{-7}$	13
PSF S	[2.5]	$1.37^{+0.18}_{-0.17}$	$10 \pm 2$	...	...	...
PWN S	[2.5]	$1.57^{+0.29}_{-0.27}$	$17 \pm 4$	$9 \pm 1$	$11 \pm 2$	1.2
PSF SW	[2.5]	$1.34^{+0.15}_{-0.15}$	$5.1^{+0.8}_{-0.7}$	...	...	...
PWN SW	[2.5]	$1.65^{+0.56}_{-0.49}$	$7.3^{+3.4}_{-2.7}$	$3 \pm 1$	$4 \pm 1$	0.4

NOTE.—The errors shown represent 90% confidence intervals. The fluxes and luminosities are for the 0.5–8 keV band.

<sup>a</sup>The region marked S is the semiannulus  $0''.75 < r < 4''$  in the semicircle south of the pointlike source, shown in the bottom page of Figure 1. The region marked SW is the southwest part,  $1'' < l < 18''$ , of the  $36'' \times 5''$  rectangle shown in the upper panel of Figure 1.

<sup>b</sup>PL normalization in units of  $10^{-6}$  photons  $\text{keV}^{-1} \text{cm}^{-2} \text{s}^{-1}$  at 1 keV.

<sup>c</sup>Observed (absorbed) flux in units of  $10^{-14}$  erg  $\text{cm}^{-2} \text{s}^{-1}$  (in  $1''$  radius aperture for the pointlike source, which contains 86% energy fraction).

<sup>d</sup>Unabsorbed flux in units of  $10^{-14}$  erg  $\text{cm}^{-2} \text{s}^{-1}$  (aperture-corrected for the pointlike source).

<sup>e</sup>Luminosity in units of  $10^{32} d_3^2$  erg  $\text{s}^{-1}$ .